Intrinsic planar polarity mechanisms influence the position-dependent regulation of synapse properties in inner hair cells

Philippe Jean[a,b,c,d,e], Özge Demet Özçete[a,b,c,e,f], Basile Tarchini[g,h,i,1], and Tobias Moser[a,b,c,e,j,1]

[a]Institute for Auditory Neuroscience, University Medical Center Göttingen, 37075 Göttingen, Germany; [b]InnerEarLab, University Medical Center Göttingen, 37075 Göttingen, Germany; [c]Collaborative Research Center 889, University of Göttingen, 37075 Göttingen, Germany; [d]Göttingen Graduate School for Neurosciences and Molecular Biosciences, University of Göttingen, 37075 Göttingen, Germany; [e]Auditory Neuroscience Group, Max Planck Institute for Experimental Medicine, 37075 Göttingen, Germany; [f]International Max Planck Research School Neuroscience, Göttingen Graduate School for Neuroscience and Molecular Biosciences, University of Göttingen, 37073 Göttingen, Germany; [g]The Jackson Laboratory, Bar Harbor, ME 04609; [h]Department of Medicine, Tufts University, Boston, MA 02111; [i]Graduate School of Biomedical Science and Engineering, University of Maine, Orono, ME 04469; and [j]Center for Nanoscale Microscopy and Molecular Physiology of the Brain, University Medical Center Göttingen, 37075 Göttingen, Germany

Edited by Robert H. Edwards, University of California, San Francisco, CA, and approved March 19, 2019 (received for review November 2, 2018)

Encoding the wide range of audible sounds in the mammalian cochlea is collectively achieved by functionally diverse type I spiral ganglion neurons (SGNs) at each tonotopic position. The firing of each SGN is thought to be driven by an individual active zone (AZ) of a given inner hair cell (IHC). These AZs present distinct properties according to their position within the IHC, to some extent forming a gradient between the modiolar and the pillar IHC side. In this study, we investigated whether signaling involved in planar polarity at the apical surface can influence position-dependent AZ properties at the IHC base. Specifically, we tested the role of Gαi proteins and their binding partner LGN/Gpsm2 implicated in cytoskeleton polarization and hair cell (HC) orientation along the epithelial plane. Using high and superresolution immunofluorescence microscopy as well as patch-clamp combined with confocal Ca^{2+} imaging we analyzed IHCs in which Gαi signaling was blocked by Cre-induced expression of the pertussis toxin catalytic subunit (PTXa). PTXa-expressing IHCs exhibited larger $Ca_V1.3$ Ca^{2+}-channel clusters and consequently greater Ca^{2+} influx at the whole-cell and single-synapse levels, which also showed a hyperpolarized shift of activation. Moreover, PTXa expression collapsed the modiolar–pillar gradients of ribbon size and maximal synaptic Ca^{2+} influx. Finally, genetic deletion of *Gαi3* and *LGN/Gpsm2* also disrupted the modiolar–pillar gradient of ribbon size. We propose a role for Gαi proteins and LGN in regulating the position-dependent AZ properties in IHCs and suggest that this signaling pathway contributes to setting up the diverse firing properties of SGNs.

hearing | sound encoding | ribbon synapse | Ca signal | Gαi protein

The sense of hearing relies on vivid, temporally precise, and tireless encoding of sounds ranging in pressure over six orders of magnitude. Active amplification of cochlear vibrations for soft sounds and compression at strong ones enable the inner hair cell (IHC) receptor potential to represent the broad range of audible sound pressures (1). Each IHC forms ribbon synapses with several type I spiral ganglion neurons (SGNs) that relay the auditory information to the brainstem. Each of the functionally diverse SGNs only encodes a fraction of the audible range of sound pressures. Collectively, they cover the entire dynamic range: high-spontaneous rate, low-sound threshold SGNs (high SR) encode soft sounds, and low-spontaneous rate, high-threshold SGNs (low SR) encode loud sounds (2–4). Since such functionally diverse SGNs can exhibit comparable frequency tuning, they are thought to receive input from neighboring or even the same IHC at a given tonotopic position (2, 5, 6). Based on back-tracing experiments it was proposed that low-SR SGNs preferentially contact the modiolar side of the IHCs, facing the spiral ganglion, while high-SR SGNs are more likely to target the pillar side of the IHCs, facing the outer hair cells (OHCs) (6).

Several mechanisms have been proposed to explain the different SGN firing patterns. Postsynaptic morphology shows different fiber caliber and mitochondrial content (6) as well as different amounts of AMPA receptors (7–9). The lateral olivocochlear system could provide differential efferent modulation (7, 10). Finally, presynaptic mechanisms could establish the different firing properties of SGNs (6, 11–14), where larger ribbons associated with more synaptic vesicles and Ca^{2+} channels are found at modiolar active zones (AZs) likely facing low-SR SGNs (6, 11–14). How larger AZs, likely having greater maximal synaptic strength, could drive low-SR SGNs remained a mystery until it was discovered that their Ca^{2+} influx seems to operate at more depolarized potentials than that of AZs of the pillar side (14). This could readily explain the higher spontaneous rate and lower sound threshold of the SGNs contacting the pillar AZs, where substantial release is expected at the resting potential of IHCs and small receptor potentials might suffice to increase the release rate (14). However, how the IHC manages to diversify AZs to decompose the full auditory information contained in the receptor potential into different neural channels remains largely unclear. Nonmutually exclusive candidate mechanisms for the

Significance

The wide dynamic range of sound encoding enables perception of sounds varying over six orders of magnitude, thought to be collectively achieved by distinct classes of type I spiral ganglion neurons (SGNs) contacting each inner hair cell (IHC). These synaptic contacts have been shown to vary according to the SGN firing properties along the modiolar–pillar axis. It has also been shown that the IHCs spatially segregate active zones (AZs) with different Ca^{2+}-influx properties, proposing an attractive candidate mechanism for the diverse sound encoding properties among SGNs. Our study, combining confocal/STED immunofluorescence microscopy, patch-clamp, and Ca^{2+} imaging, proposes that Gαi and LGN, involved in planar polarity mechanisms at the IHC apex, contribute to establish the spatial gradient of IHC AZ properties.

Author contributions: P.J., B.T., and T.M. designed research; P.J., Ö.D.Ö., and B.T. performed research; P.J. and Ö.D.Ö. analyzed data; and P.J., Ö.D.Ö., B.T., and T.M. wrote the paper.

The authors declare no conflict of interest.

This article is a PNAS Direct Submission.

[1]To whom correspondence may be addressed. Email: basile.tarchini@jax.org or tmoser@gwdg.de.

This article contains supporting information online at www.pnas.org/lookup/suppl/doi:10.1073/pnas.1818358116/-/DCSupplemental.

Published online April 11, 2019.

observed spatial gradients of AZ properties include (*i*) a cell autonomous signaling mechanism in IHCs or an instructive influence by (*ii*) SGNs or (*iii*) efferent innervation.

Here we explored the exciting possibility that planar polarity mechanisms responsible for establishing the proper architecture of the hair bundles and their uniform orientation across HCs (15–17) also instruct the observed basolateral gradients of IHC synapse properties. During early development, the apical HC compartment located between the tallest stereocilia and the abneural junctions of the cell (the bare zone) lacks protrusions and hosts the polarized localization of Insc, LGN/Gpsm2, and Gαi (18). This protein complex was first shown to control mitotic spindle orientation and thereby asymmetric cell division in *Drosophila*, a function broadly conserved in mammals (19). Gαi-LGN exclude aPKC, and the resulting compartmentalization of the HC apex influences the position of the kinocilium and the stereocilia, shaping cytoskeleton intrinsic asymmetry and possibly aligning it with tissue-wide polarity cues residing at cell–cell junctions, including core planar cell polarity (PCP) proteins (18, 20, 21). Moreover, LGN and Gαi are also enriched at the tips of the tallest stereocilia (22–24), making the Insc-LGN-Gαi complex a promising candidate for conveying information across compartments (23). Pertussis toxin (PTX) is well known to ADP ribosylate and block Gαi signaling, and interestingly, PTX application led to PCP defects and a deficit of kinocilium migration in HCs in cochlear cultures (20). Moreover, transgenic or Cre-induced expression of PTX catalytic subunit (PTXa) in HC in vivo induced PCP defects, stereocilia stunting, and severe hair bundle disorganization associated to profound deafness (18, 23). *LGN* mutants shared stereocilia stunting and profound deafness (22–25), while milder hair bundle defects and hearing loss were reported in mutant mice lacking Gαi3 (22), and these phenotypes were accentuated in conditional double *Gαi2*/*Gαi3* mutants (25). Neither *LGN* nor single *Gαi3* mutants recapitulate the severe PCP defects observed in PTXa-expressing HCs, presumably because of functional redundancy among Gαi proteins (18, 20).

Here we combined morphological and physiological analysis of mouse IHCs expressing PTXa (23) and found that the disruption of Gαi signaling affects the properties and spatial heterogeneity of the AZs in IHCs. Confocal and stimulated emission depletion (STED) microscopy showed that the mutant synapses were unchanged in number but were reorganized with larger and more complex Ca^{2+}-channel clusters and a loss of the modiolar–pillar gradient of ribbon size. Performing patch-clamp and live confocal Ca^{2+} imaging, we showed that the mutant IHCs exhibited an increased amplitude and hyperpolarized activation of Ca^{2+} influx at the whole-cell and single-synapse levels. Moreover, the modiolar–pillar gradient for synaptic Ca^{2+} influx strength observed in control condition was collapsed in PTXa-expressing IHCs. The gradient of ribbon size was also disrupted in *Gαi3* and *LGN* KOs, suggesting that HC-intrinsic mechanisms influencing planar polarity at the apical membrane might also regulate the modiolar–pillar distribution of ribbon synapse properties.

Results

The Modiolar–Pillar Gradient of Ribbon Size Is Dependent on Gαi Function. Organs of Corti from 3-wk-old control (*Atoh1-Cre*- or PTXa-negative, referred to as PTXa controls) and *Atoh1-Cre; $PTXa^{fl/fl}$* mice (referred to as PTXa mutants) were processed in parallel for immunohistochemistry. As previously reported (23), PTXa-expressing IHCs presented disorganized and shortened hair bundles. Moreover, they occasionally showed a misplaced basal body indicated by the position of the fonticulus/cytoplasmic channel in phalloidin stainings of F-actin, demonstrating that planar orientation defects most severe in OHCs (18) can also affect IHCs. In control IHCs, the fonticuli were invariably located toward the pillar side of the cell, indicating a correct apical IHC orientation. Interestingly, most misoriented mutant IHCs showed a diametrically opposite position of the fonticulus toward the modiolus (180° inversion; Fig. 1*A*).

Next, we combined F-actin labeling to record IHC orientation with immunostaining against Otoferlin or Vglut3 to outline the IHC shape and CtBP2/RIBEYE to estimate the localization of the ribbons and approximate their size. Thereby, we investigated whether the altered apical orientation might go along with a change of the previously reported modiolar–pillar gradient of ribbon size in IHCs (14, 27). For analysis, we reconstructed the IHCs in cylindrical coordinates to overlay multiple cells and study the position dependence of ribbon size (*SI Appendix*, *SI Materials and Methods*). As expected, in IHCs of PTXa control littermates, the modiolar–pillar gradient of RIBEYE-immunofluorescence intensity [proxy of ribbon size (28), normalized to the mean modiolar RIBEYE immunofluorescence intensity] was observed [modiolar, 1.00 ± 0.03 (SD = 0.40), *n* (number of replicates) = 211 AZs vs. pillar, 0.82 ± 0.03 (SD = 0.34), *n* = 148 AZs in 22 IHCs, N (number of animals) = 5, $P < 0.00001$, Mann–Whitney–Wilcoxon test] (Fig. 1 *B* and *C*, in black). Initially, we considered using PTXa-expressing, noninverted IHCs as internal controls. Interestingly, however, we observed a complete collapse of the ribbon size gradient upon PTXa expression regardless of apical IHC orientation [PTXa mutant noninverted, in blue, modiolar, 1.00 ± 0.03 (SD = 0.35), *n* = 190 AZs vs. pillar, 0.99 ± 0.03 (SD = 0.35), *n* = 171 AZs in 22 IHCs, N = 12, $P = 0.88$; PTXa mutant 180° inverted, in red, modiolar, 1.00 ± 0.02 (SD = 0.31), *n* = 192 AZs vs. pillar, 0.95 ± 0.02 (SD = 0.31), *n* = 174 AZs in 22 IHCs, N = 12, $P = 0.75$, Mann–Whitney–Wilcoxon test for both conditions] (Fig. 1 *B* and *C*).

To enhance the specificity of our manipulation, we turned to mutants constitutively lacking either Gαi2 or Gαi3. Both littermate controls and homozygote mutants lacking Gαi2 exhibited a modiolar–pillar gradient of RIBEYE-immunofluorescence [$Gαi2^{KO/KO}$, modiolar, 1.00 ± 0.03 (SD = 0.38), n = 220 AZs vs. pillar, 0.64 ± 0.02 (SD = 0.26), *n* = 107 AZs vs. $Gαi2^{+/+}$ or $Gαi2^{KO/+}$, modiolar, 1.00 ± 0.03 (SD = 0.43), *n* = 213 AZs vs. pillar, 0.77 ± 0.03 (SD = 0.31), *n* = 114 AZs; in 18 IHCs for N = 4 for both conditions, $P < 0.00001$, Mann–Whitney–Wilcoxon test] (*SI Appendix*, Fig. S1*A*). However, deleting Gαi3 collapsed the modiolar–pillar gradient of ribbon size [$Gαi3^{KO/KO}$, modiolar, 1.00 ± 0.02 (SD = 0.36), *n* = 218 AZs vs. pillar, 1.04 ± 0.03 (SD = 0.38), *n* = 145 AZs, $P = 0.24$ vs. $Gαi3^{KO/+}$, modiolar, 1.00 ± 0.02 (SD = 0.33), *n* = 225 AZs vs. pillar, 0.76 ± 0.02 (SD = 0.27), *n* = 143 AZs; in 20 IHCs for N = 5 for both conditions, $P < 0.00001$, Mann–Whitney–Wilcoxon test] (Fig. 2*A*). Interestingly, constitutive inactivation of LGN/Gpsm2, a direct binding partner of Gαi3, also collapsed the gradient of ribbon size [$LGN^{KO/KO}$, modiolar, 1.00 ± 0.02 (SD = 0.35), *n* = 231 AZs vs. pillar, 0.96 ± 0.03 (SD = 0.36), *n* = 184 AZs, $P = 0.11$ vs. $LGN^{KO/+}$, modiolar, 1.00 ± 0.02 (SD = 0.36), *n* = 298 AZs vs. pillar, 0.75 ± 0.02 (SD = 0.27), *n* = 128 AZs; in 24 IHCs for N = 4 for both conditions, $P < 0.00001$, Mann–Whitney–Wilcoxon test] (Fig. 2*B*). Together, these results suggest that the Gαi-LGN complex previously shown to affect cell polarity during apical HC morphogenesis is also critical to establish the modiolar–pillar gradient of ribbon synapse size in IHCs.

Downregulating Gαi activity in HCs with PTXa, inactivating both Gαi2 + Gαi3 or inactivating LGN resulted in profound deafness in young adults already (22–26). To explore the possibility that the disruption of the modiolar–pillar gradient of ribbon size is consecutive to the loss of sound-evoked synaptic activity, we turned to $Myo15^{sh2}$ mice. $Myo15^{sh2}$ HCs show normal planar architecture and orientation but like PTXa and LGN mutants exhibit disorganized and shortened hair bundles associated with complete deafness (29). $Myo15^{sh/sh2}$ IHCs retained a significant modiolar–pillar gradient of ribbon size [$Myo15^{sh/sh2}$, modiolar, 1.00 ± 0.05 (SD = 0.65), *n* = 173 AZs vs. pillar, 0.66 ± 0.04 (SD = 0.62), *n* = 133 AZs vs. $Myo15^{sh2/+}$ controls, modiolar, 1.00 ± 0.03 (SD = 0.37), *n* = 203 AZs vs. pillar, 0.73 ± 0.02 (SD = 0.23), *n* = 193 AZs in 21 IHCs for N = 3 for both conditions, $P < 0.00001$, Mann–Whitney–Wilcoxon test] (*SI Appendix*, Fig. S1*B*). This indicates that altered mechanoelectrical

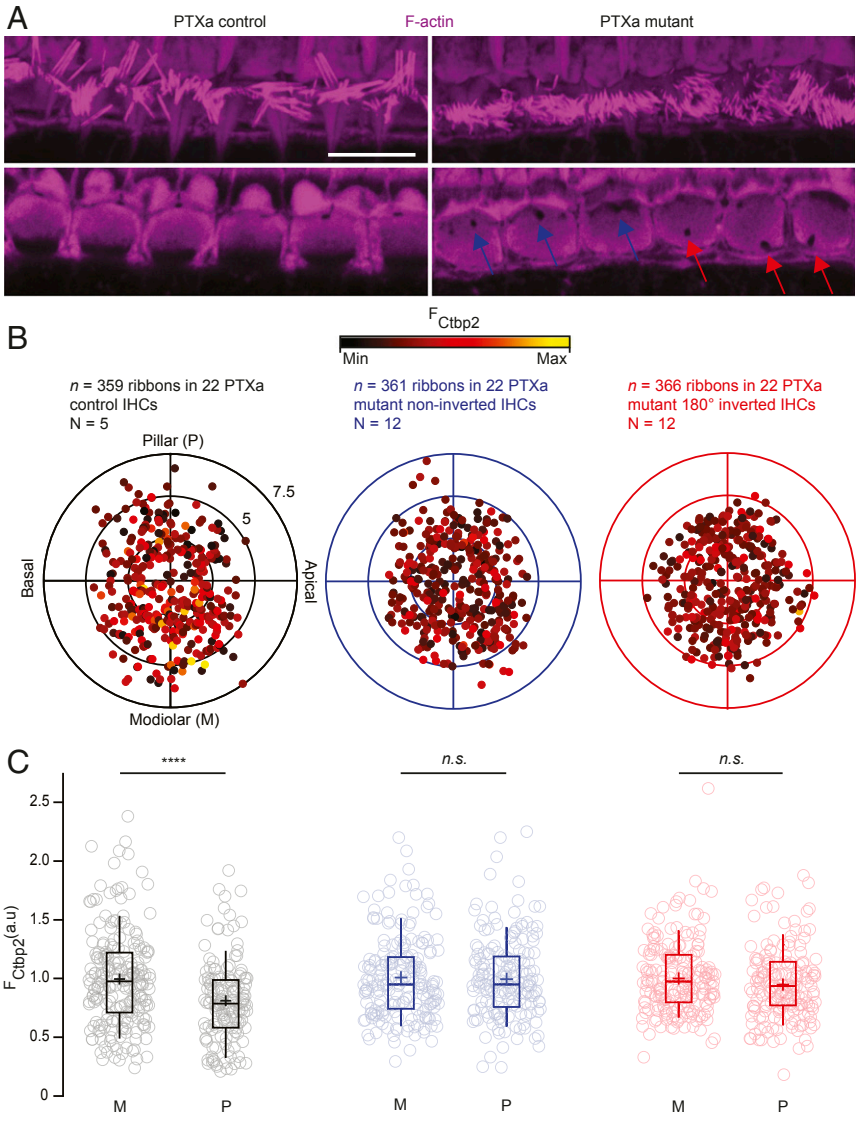

Fig. 1. Blocking Gαi signaling by PTXa expression in IHCs disrupts the modiolar–pillar gradient for ribbon size. (*A*) Maximal projection (*Top*) and single confocal section (*Bottom*) of the IHC cuticular plates stained with phalloidin marking F-actin. The immunostainings reveal the shortened and disorganized hair bundles in the PTXa mutant organ of Corti, as well as the misplaced fonticulus/cytoplasmic channel indicating the position of the basal body (blue arrows for PTXa mutant noninverted cells and red arrows for PTXa mutant 180° inverted cells). (Scale bar: 10 μm.) (*B*) The polar charts (black for PTXa control, blue for PTXa mutant noninverted cells, and red for PTXa mutant 180° inverted cells) display locations and intensities of immunofluorescently labeled CtBP2 marking the ribbons. Modiolar and pillar refer to facing toward or away from the ganglion in the modiolus; apical and basal refer to the tonotopic axis of the organ of Corti. The fluorescence intensity of each CtBP2 signal point is reflected by its color, with warmer, yellow tones indicating higher intensity and cooler, darker tones indicating lower intensity. Each radial circle is 2.5 μm. (*C*) The IHCs from PTXa control condition display a significant gradient with stronger ribbons in the modiolar side (M) compared with the pillar side (P) [PTXa control (black), modiolar, $n = 211$ AZs vs. pillar, $n = 148$ AZs, $P < 0.00001$, Mann–Whitney–Wilcoxon test]. This gradient collapsed completely in the PTXa mutant IHCs regardless of the fonticulus position [PTXa mutant noninverted (blue), modiolar, $n = 190$ AZs vs. pillar, $n = 171$ AZs, $P = 0.88$; PTXa mutant 180° inverted (red), modiolar, $n = 192$ AZs vs. pillar, $n = 174$ AZs, $P = 0.75$, Mann–Whitney–Wilcoxon test for both conditions]. Box plots show 10th, 25th, 50th, 75th, and 90th percentiles with individual data points overlaid; means are shown as crosses.

transduction resulting from stunted stereocilia is not the primary cause for the lost gradient of ribbon size observed in IHCs lacking Gαi-LGN function.

Inactivating Gαi Reorganizes and Potentiates Ca^{2+} Influx at IHC AZs. Next, we performed a detailed immunofluorescence analysis of ribbon synapse morphology in PTXa-expressing IHCs. We stained against CtBP2/RIBEYE and found no significant differences between PTXa control and mutant conditions for the average number of ribbons per IHC [PTXa mutant, 12.41 ± 0.43 (SD = 2.12) vs. PTXa control, 12.54 ± 0.29.(SD = 1.44); $n = 24$ IHCs, N = 6, $P = 0.81$, *t* test] or their mean RIBEYE immunofluorescence intensity [PTXa mutant, 6.51 ± 0.13 a.u. (SD = 2.49 a.u.), $n = 360$ AZs, N = 9 vs. PTXa control, 6.62 ± 0.13 a.u. (SD = 2.26 a.u.); $n = 327$ AZs; N = 9, $P = 0.28$, Mann–Whitney–Wilcoxon] (*SI Appendix*, Fig. S2 *A–C*). Next, we labeled $Ca_V1.3$ Ca^{2+} channels, contributing more than 90% of the voltage-gated Ca^{2+} influx in IHCs (30–32). Using confocal microscopy, presynaptic Ca^{2+}-channel clusters were identified as spots of $Ca_V1.3$ immunofluorescence juxtaposed to the postsynaptic density (PSD) detected as PSD-95 immunofluorescent spots. $Ca_V1.3$ channels remained clustered at mutant AZs and were further quantified by fitting $Ca_V1.3$ immunofluorescent spots with a 2D Gaussian function. The amplitudes of the fits in PTXa-expressing IHCs were significantly greater for $Ca_V1.3$ [PTXa mutant, 0.74 ± 0.03 a.u.

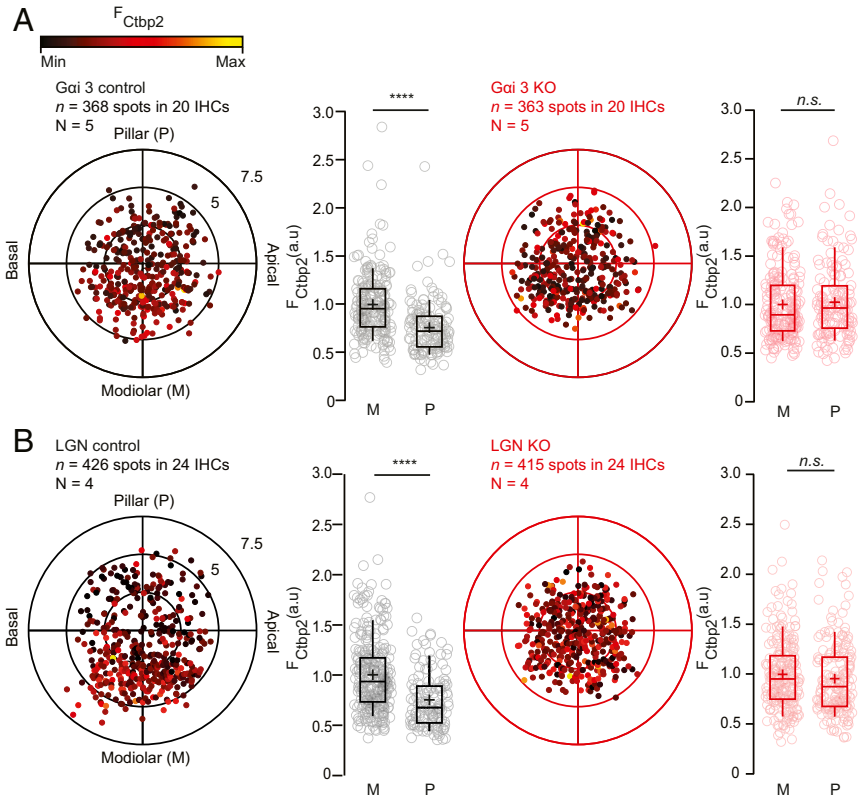

Fig. 2. Inactivating *Gαi3* or *LGN* collapses the modiolar–pillar gradient for ribbon size. (*A*) The polar charts display locations and intensities of immunofluorescently labeled CtBP2 marking the ribbons. Modiolar and pillar refer to facing toward or away from the ganglion in the modiolus; apical and basal refer to the tonotopic axis of the organ of Corti. The fluorescence intensity of each CtBP2 signal point is reflected by its color, with warmer, yellow tones indicating higher intensity and cooler, darker tones indicating lower intensity. The spatial gradient for ribbon strength was lost upon *Gαi3* inactivation (modiolar, n = 218 AZs vs. pillar, *n* = 145 AZs for 20 IHCs, N = 5, $P < 0.00001$, Mann–Whitney–Wilcoxon test), whereas it was preserved in the heterozygote littermate controls (modiolar, *n* = 225 AZs vs. pillar, *n* = 143 AZs in 20 IHCs, *n* = 5, $P < 0.00001$, Mann–Whitney–Wilcoxon test). Box plots show 10th, 25th, 50th, 75th, and 90th percentiles with individual data points overlaid; each radial circle is 2.5 μm, and means are shown as crosses as for *B*. (*B*) The inactivation of *LGN* collapsed the gradient of ribbon size [*LGN KO*, modiolar, *n* = 231 AZs vs. pillar, *n* = 184 AZs, $P = 0.11$ vs. *LGN control* (heterozygotes), *n* = 298 AZs vs. pillar, *n* = 128 AZs, $P < 0.00001$; 24 IHCs, *n* = 4, Mann–Whitney–Wilcoxon test for both conditions].

(SD = 0.38 a.u.) vs. PTXa control, 0.52 ± 0.03 a.u. (SD = 0.27 a.u.); *n* = 118, N = 6 for both genotypes, $P < 0.00001$, Mann–Whitney–Wilcoxon test]. This was the case also for PSD-95 [PTXa mutant, 0.37 ± 0.02 a.u. (SD = 0.20 a.u.)] vs. PTXa control, 0.28 ± 0.01 a.u. (SD = 0.15 a.u.); *n* = 118, N = 6 for both conditions, $P = 0.0009$ and Mann–Whitney–Wilcoxon test) (Fig. 3 *A* and *B*). Interestingly, we observed a strong positive correlation between the immunofluorescence intensities for $Ca_V1.3$ and its associated PSD-95 in PTXa control IHCs (Pearson coefficient of 0.74, $P < 0.00001$). This correlation was weaker for PTXa mutant IHCs (Pearson coefficient of 0.36, $P < 0.001$) (*n* = 100 spots, N = 5 for both conditions) (Fig. 3*C*), indicating that the scaling of presynaptic densities with PSD size is impaired upon PTXa expression. In agreement with the enlarged PSDs in the mutant condition, the GluA3 immunofluorescent spots [indicating the postsynaptic AMPA receptor (AMPAR) clusters] showed a significantly increased intensity [PTXa mutant, 0.85 ± 0.03 a.u. (SD = 0.28 a.u.) vs. PTXa control, 0.74 ± 0.02 a.u. (SD = 0.23 a.u.); *n* = 120, N = 4 for both genotypes, $P < 0.00001$, Mann–Whitney–Wilcoxon test], while they maintained their ring-like shape (*SI Appendix*, Fig. S3 *A* and *B*).

To analyze the spatial organization of synaptic Ca^{2+} channels, we performed two-color, 2D-STED imaging of $Ca_V1.3$ and PSD-95 immunofluorescence. $Ca_V1.3$ clusters were categorized according to their arrangements and number of structures (33, 34) (Fig. 3 *D* and *E*). PTXa control and mutant IHCs exhibited comparable proportions of point-like clusters [9 and 10%, respectively; characterized by a Gaussian fitting ratio full width half maximum (FWHM) long axis/FWHM short axis <2; purple]. While ∼40% of the control AZs showed the typical line-like organization of $Ca_V1.3$ immunofluorescence (defined by a width inferior to 140 nm; red), these structures were rare in mutant IHCs with a prevalence of only 8%. However, the fat line-like clusters, defined as lines wider than 140 nm (blue), had equivalent prevalence in both control (23%) and mutant (27%) conditions. Importantly, PTXa-expressing IHCs showed a greater proportion of complex clusters (55%), defined by two or more $Ca_V1.3$ immunofluorescent structures at the synapse, than control IHCs (26%). Moreover, while these complex arrangements exhibited up to two or three structures in the control AZs, they could present up to five in the mutant ones (Fig. 3 *D* and *E*). Accordingly, the average number of $Ca_V1.3$-immunofluorescent spots was significantly higher at synapses of PTXa-expressing IHCs compared with control ones [PTXa mutant, 2.10 ± 0.11 (SD = 1.26) vs. PTXa control, 1.34 ± 0.06 (SD = 0.61), *n* = 120 synapses, N = 3 for both conditions; $P < 0.00001$, Mann–Whitney–Wilcoxon test]. This difference was most probably underestimated due to the low resolution of 2D-STED in the *z* axis. The greater number of $Ca_V1.3$-immunofluorescent spots at STED resolution is consistent with the stronger $Ca_V1.3$-immunofluorescence intensity observed at the confocal level (Fig. 3 *A* and *B*). Altogether, these data suggest that PTXa-expressing IHCs possess normally sized ribbons, whereas $Ca_V1.3$ Ca^{2+} channels are organized in larger and more complex clusters, juxtaposed to larger PSDs compared with controls.

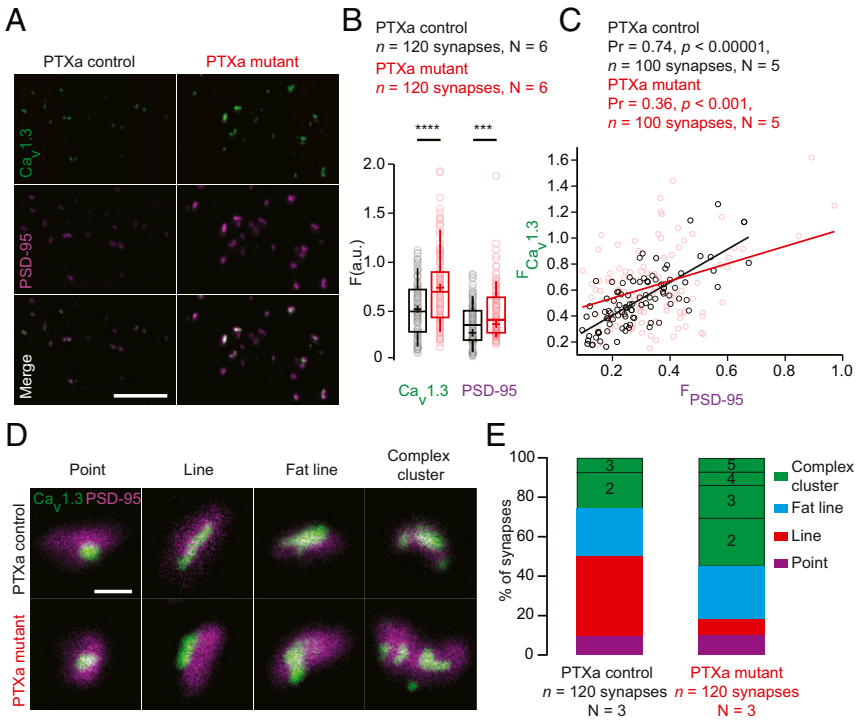

Fig. 3. PTXa-expressing IHCs exhibit enlarged $Ca_V1.3$ channel and PSD-95 clusters. (*A*) Maximum intensity projections of confocal sections from organs of Corti immunolabeled for $Ca_V1.3$ Ca^{2+} channels and PSD-95. (Scale bar: 5 μm.) (*B*) Mean immunofluorescence intensities of synaptic $Ca_V1.3$ Ca^{2+}-channel clusters and PSD-95 (estimated by the maximal amplitude of 2D Gaussian fits) were significantly increased in the PTXa mutant IHCs (red circles) compared with PTXa control IHCs (black circles) (n = 120 synapses; N = 6 for both conditions; $P < 0.00001$ and $P = 0.0009$ for $Ca_V1.3$ and PSD-95 spots, respectively; Mann–Whitney–Wilcoxon test for both conditions). (*C*) Scatter plot displaying the immunofluorescence intensities of $Ca_V1.3$ spots against their associated PSD-95 spots. A positive correlation is found in the PTXa control condition (black circles, Pearson coefficient of 0.74, $P < 0.00001$, n = 100 synapses, N = 5), while the correlation is much weaker in the PTXa mutant IHCs (red circles, Pearson correlation coefficient of 0.36, $P < 0.001$, n = 100 synapses, N = 5). (*D*) Representative examples of AZs immunolabeled against $Ca_V1.3$ Ca^{2+} channels and PSD-95, acquired with 2D-STED microscopy. AZs from both conditions exhibited point-like clusters (defined by a Gaussian fitting ratio L.A./S.A. < 2); some clusters formed lines (defined by an S.A. < 140 nm), fat lines (defined by an S.A. > 140 nm), and complex arrangements (defined by two or more structures). (Scale bar: 500 nm.) (*E*) The $Ca_V1.3$ Ca^{2+}-channel clusters were categorized according to these arrangements. PTXa control and mutant IHCs exhibited similar proportions of point-like clusters (9 and 10%, respectively; violet). Around 40% of the control AZs showed the typical line-like organization of $Ca_V1.3$ immunofluorescence; these structures were more sporadic in mutant IHCs (8%; red). However, the fat line clusters (blue) had comparable prevalence in both PTXa control (23%) and mutant (27%) conditions. Strikingly, a difference was found for the proportion of complex clusters that were much more frequent in the PTXa mutant condition (55% against 26% in the PTXa control IHCs). Additionally, these features exhibited up to three structures at the control AZs, while the mutant ones could present up to five (n = 120 synapses, N = 3 for both conditions).

Inactivating Gαi Causes an Increased Amplitude and Hyperpolarized Activation of IHC Ca^{2+} Influx. To physiologically characterize the effect of inactivating Gαi on $Ca_V1.3$ Ca^{2+} channels, we first recorded the whole-cell Ca^{2+} current of PTXa-expressing IHCs in the ruptured-patch configuration (5 mM $[Ca^{2+}]_e$; Fig. 4*A*). The amplitude of the Ca^{2+} influx (Fig. 4, A_i) was substantially increased in PTXa-expressing IHCs [PTXa mutant, −276 ± 8 pA (SD = 50 pA), n = 40 IHCs, N = 13 vs. PTXa control, −191 ± 6 pA, SD = 38 pA, n = 40 IHCs, N = 14; $P < 0.00001$, t test], consistent with the more numerous $Ca_V1.3$ channels indicated by immunohistochemistry. Next, we analyzed the voltage dependence of Ca^{2+}-channel activation (Fig. 4*B*) and found a significant hyperpolarizing shift of −4 mV of the voltage of half-maximal Ca^{2+}-channel activation, V_h [Fig. 4, B_i; PTXa mutant, −28.16 ± 0.54 mV (SD = 3.41 mV), n = 40 IHCs, N = 13 vs. PTXa control, −24.34 ± 0.46 mV (SD = 2.93 mV), n = 40 IHCs, N = 14, $P < 0.00001$, t test]. Moreover, we found a subtle but significant increase of the voltage sensitivity of activation (apparent as a decrease of the slope factor k) in mutant IHCs [PTXa mutant, 7.33 ± 0.06 mV (SD = 0.41 mV), n = 40 IHCs, N = 13 vs. PTXa control, 7.72 ± 0.07 mV (SD = 0.42 mV), n = 40 IHCs, N = 14, $P < 0.00001$, t test; Fig. 4, B_{ii}].

To test the consequences of the $Ca_V1.3$ Ca^{2+} channel rearrangement in the PTXa mutant IHCs on exocytosis, we performed membrane capacitance measurements (C_m) in the perforated patch-clamp configuration (1.3 mM $[Ca^{2+}]_e$; Fig. 4 *C*–*H*). IHCs were step depolarized to −17 mV for different durations (2 to 50 ms) to probe the vesicle pool dynamics. Consistent with the above results, the integrated Ca^{2+} influx [Ca^{2+} charge (Q_{Ca})] of the PTXa mutant IHCs was significantly increased for every pulse duration tested (Q_{Ca} at 2 ms, P = 0.002; Q_{Ca} at 5 ms, P = 0.004; Q_{Ca} at 10 ms, P = 0.004; Q_{Ca} at 20 ms, P = 0.01; Q_{Ca} at 50 ms, P = 0.01, n = 10 IHCs, N = 7 in the PTXa mutant; n = 10 IHCs, N = 6 in the PTXa control; t test; Fig. 4*D*). Surprisingly, despite the significantly increased Ca^{2+} influx, the PTXa mutant IHCs tended to have smaller exocytic C_m changes (ΔC_m) for short stimulus durations that are thought to primarily reflect the readily releasable pool of vesicles (RRP, ΔC_m at 2 ms, P = 0.02, t test; at 10 ms, P = 0.03, Mann–Whitney–Wilcoxon test). Sustained exocytosis of IHCs was probed with 50-ms step depolarization, which yielded comparable ΔC_m. The ratio of ΔC_m over Q_{Ca}, i.e., the efficiency of Ca^{2+} influx to drive exocytosis, was reduced for all depolarization durations tested in PTXa mutant IHCs (n = 10 IHCs, N = 7 in the PTXa mutant; n = 10 IHCs, N = 6 in the PTXa control; for ratio at 2 ms, P = 0.02; at 5 ms, P = 0.01; at 10 ms, 0.006; at 20 ms, P = 0.001; Q_{Ca} at 50 ms, P = 0.005, t test; Fig. 4*E*). Possible reasons include an impaired coupling of Ca^{2+} channels to vesicular release sites, which seems plausible given the disarrangement of the $Ca_V1.3$ Ca^{2+} channel clusters (Fig. 3 *D* and *E*). However, we cannot exclude a contribution of other mechanisms such as a putative saturation of the

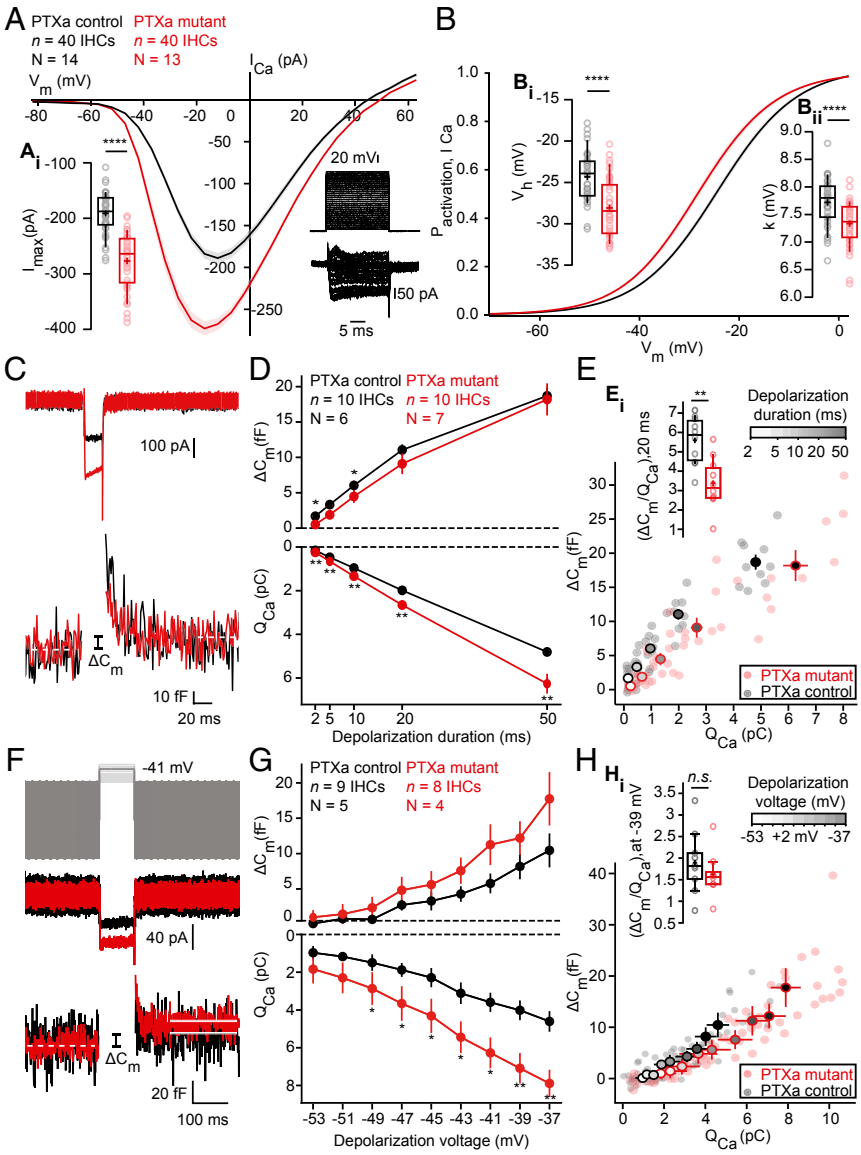

Fig. 4. PTXa-expressing IHCs show an increased and hyperpolarized Ca^{2+} influx at the whole-cell level. (*A*) IV relationship of the whole-cell Ca^{2+} current (ruptured-patch configuration, 5 mM $[Ca^{2+}]_e$) shows a significantly increased current amplitude in the PTXa mutant IHCs ($n = 40$ IHCs, N = 13 in the PTXa mutant; $n = 40$ IHCs, N = 14 in the PTXa control; $P < 0.0001$, *t* test) (*A*$_i$). The protocol, consisting of 20-ms steps of 5 mV from −82 to +63 mV, as well as the resulting currents of a representative control IHC, are shown in the *Bottom Right*. Mean (line) ± SEM (shaded areas) are displayed; the box plots show 10th, 25th, 50th, 75th, and 90th percentiles with individual data points overlaid, and means are shown as crosses, as for *B*. (*B*) Fractional activation of the whole-cell Ca^{2+} current derived from the IV relationships (*A*) was fitted to a Boltzmann function. (*B*$_i$) Box plots of the voltage for half-maximal activation V_h and V_h estimates of individual IHCs show a significant hyperpolarized shift of the fractional activation (V_h) of the $Ca_V1.3$ Ca^{2+} channels in the PTXa mutant condition ($n = 40$ IHCs, N = 13 in the PTXa mutant; n = 40 IHCs, N = 14 in the PTXa control; $P < 0.0001$, *t* test). (*B*$_{ii}$) Box plots of the voltage sensitivity or slope factor k and k estimates of individual IHCs illustrate increased voltage sensitivity in the PTXa mutant condition ($n = 40$ IHCs, $n = 13$ in the mutant; $n = 40$ IHCs, N = 14 in the PTXa control; $P < 0.0001$, *t* test). (*C*) Representative Ca^{2+} currents (*Top*) and corresponding low-pass filtered capacitance (*Bottom*) traces recorded from PTXa mutant and control IHCs in response to 20-ms step depolarization to −17 mV from the holding potential of −87 mV (perforated-patch configuration, 1.3 mM $[Ca^{2+}]_e$). The PTXa mutant IHCs showed bigger Ca^{2+} currents than the control IHCs, while the capacitance jumps (ΔC_m) were comparable. (*D*) Mean exocytic ΔC_m (*Top*) and Ca^{2+} current integrals (Q_{Ca}) (*Bottom*) as a function of depolarization duration (mean ± SEM, $n = 10$ IHCs, N = 7 in the PTXa mutant; $n = 10$ IHCs, N = 6 in the PTXa control; for Q_{Ca} at 2 ms, $P = 0.002$; for Q_{Ca} at 5 ms, $P = 0.005$; for Q_{Ca} at 10 ms, $P = 0.003$; for Q_{Ca} at 20 ms, $P = 0.007$; for Q_{Ca} at 50 ms, $P = 0.007$, *t* test; for ΔC_m at 2 ms, $P = 0.02$, *t* test; at 10 ms, $P = 0.03$, Mann–Whitney–Wilcoxon test). (*E*) Relation between exocytic ΔC_m and Q_{Ca} from PTXa mutant and control IHCs (mean ± SEM; fill color of the mean points darkens with increasing depolarization duration). PTXa mutant IHCs showed significantly lower efficiency of Ca^{2+} influx to drive exocytosis for every depolarization duration. (*E*$_i$) Ratio of ΔC_m and Q_{Ca} from PTXa mutant and control IHCs upon 20-ms step depolarization ($n = 10$ IHCs, N = 7 in the PTXa mutant; $n = 10$ IHCs, N = 6 in the PTXa control; for ratio at 2 ms, $P = 0.02$; at 5 ms, $P = 0.01$; at 10 ms, $P = 0.006$; at 20 ms, $P = 0.001$; Q_{Ca} at 50 ms, $P = 0.005$, *t* test). (*F*) Representative Ca^{2+} currents (*Middle*) and corresponding low-pass filtered capacitance (*Bottom*) traces recorded from PTXa mutant and control IHCs upon 100-ms step depolarization to −41 mV from the holding potential (perforated-patch configuration, 1.3 mM $[Ca^{2+}]_e$). Stimulus template (*Top*) illustrates the 2-mV steps starting from −53 to −37 mV. (*G*) Mean exocytic ΔC_m (*Top*) and Ca^{2+} current integrals (Q_{Ca}) (*Bottom*) as a function of depolarization voltage (mean ± SEM, $n = 8$ IHCs, N = 4 in the PTXa mutant; $n = 9$ IHCs, N = 5 in the PTXa control; for Q_{Ca} at −37 mV, $P = 0.002$; for Q_{Ca} at −39 mV, $P = 0.005$; for Q_{Ca} at −41 mV, $P = 0.01$, *t* test; for Q_{Ca} at −43 mV, $P = 0.02$; for Q_{Ca} at −45 mV, $P = 0.016$; for Q_{Ca} at −47 mV, $P = 0.05$; for Q_{Ca} at −49 mV, $P = 0.046$, Mann–Whitney–Wilcoxon test). (*H*) Relation between exocytic ΔC_m and Q_{Ca} from PTXa mutant and control IHCs (mean ± SEM; fill color of the mean points darkens with increasing depolarization voltage). The ratio between the ΔC_m and Q_{Ca} was comparable throughout the different voltage range (−53 to −37 mV, with 2-mV increments). (*H*$_i$) Ratio of ΔC_m and Q_{Ca} from PTXa mutant and control IHCs upon 100-ms step depolarization to −39 mV.

Ca^{2+} sensor of exocytosis. Furthermore, we have probed the voltage dependence of exocytosis given the hyperpolarized shift (−5 mV) in the activation of Ca^{2+} influx in the PTXa mutant IHCs. IHCs were step depolarized for 100 ms in the physiologically relevant voltage range, starting from −53 to −37 mV with 2-mV increments (Fig. 4*F*). PTXa mutant IHCs exhibit significantly bigger Q_{Ca} for most voltage steps, while the tendency toward larger ΔC_m did not reach statistical significance ($n = 8$ IHCs, N = 4 in the PTXa mutant; $n = 9$ IHCs, N = 5 in the PTXa control) (Fig. 4*G*). Interestingly, the ratio of ΔC_m over Q_{Ca} was comparable between PTXa mutant and control IHCs in the physiologically relevant voltage range (Fig. 4 *H* and H_i).

Next, we studied presynaptic Ca^{2+} signaling at individual AZs using spinning-disk confocal microscopy of IHCs loaded with the low-affinity Ca^{2+} indicator Fluo-4FF (800 μM), the nonfluorescent chelator EGTA (10 mM), and a TAMRA (tetramethylrhodamine)-conjugated CtBP2-binding peptide. Under these conditions the Ca^{2+} indicator fluorescence serves as a proxy of synaptic Ca^{2+} influx (12, 14, 33). AZs were identified by spots of the CtBP2-binding peptide fluorescence where Ca^{2+} signals (Fluo-4FF hotspots) commenced upon depolarization. We found an increased maximal rise of Fluo-4FF fluorescence, i.e., synaptic Ca^{2+} influx, in PTXa expressing IHCs [PTXa mutant, $\Delta F/F_{max}$, 2.05 ± 0.10 (SD = 1.34), $n = 175$ AZs vs. PTXa control, 1.59 ± 0.08 (SD = 1.10), $n = 175$ AZs; in 20 IHCs for N = 12 for both conditions, $P = 0.0002$, Mann–Whitney–Wilcoxon test; Fig. 5*A*]. This gain of synaptic Ca^{2+} influx strength agrees with the analysis of $Ca_V1.3$ immunofluorescence and with the enhanced Ca^{2+} influx at the whole-cell level. Moreover, as at the whole-cell level, we found a significant hyperpolarized shift (approximately −4 mV) of activation of the synaptic Ca^{2+} influx [PTXa mutant, V_h, −28.77 ± 0.71 mV (SD = 8.42 mV), $n = 142$ AZs in 20 IHCs, $n = 12$ vs. PTXa control, V_h, −24.11 ± 0.57 mV (SD = 6.77 mV), $n = 141$ AZs in 20 IHCs, N = 12, $P < 0.0001$, Mann–Whitney–Wilcoxon test; Fig. 5, B_i]. However, the voltage sensitivity of activation was not significantly different for the synaptic Ca^{2+} influx in PTXa-expressing IHCs likely due to higher variability at the single synapse level [PTXa mutant, k, 6.74 ± 0.17 mV (SD = 1.99 mV), $n = 142$ AZs in 20 IHCs, N = 12 vs. PTXa control, 6.81 ± 0.18 mV (SD = 2.13 mV), $n = 141$ AZs in 20 IHCs, N = 12, $P = 0.55$, Mann–Whitney–Wilcoxon test; Fig. 5 B_{ii}].

Finally, we studied the spatial extent of the synaptic Ca^{2+} signals by measuring the FWHM of 2D Gaussian function fits to the hotspots of Ca^{2+}-indicator fluorescence. We found a greater spread of synaptic Ca^{2+} signals in PTXa-expressing IHCs [PTXa mutant, long axis (L.A.) = 1,061 ± 21 nm (SD = 266 nm), short axis (S.A.) = 779 ± 18 nm (SD = 228 nm); $n = 162$ AZs in 20 IHCs, N = 12 vs. PTXa control, L.A. = 909 ± 20 nm (SD = 252 nm); S.A. = 672 ± 17 nm (SD = 218 nm), $n = 160$ AZs in 20

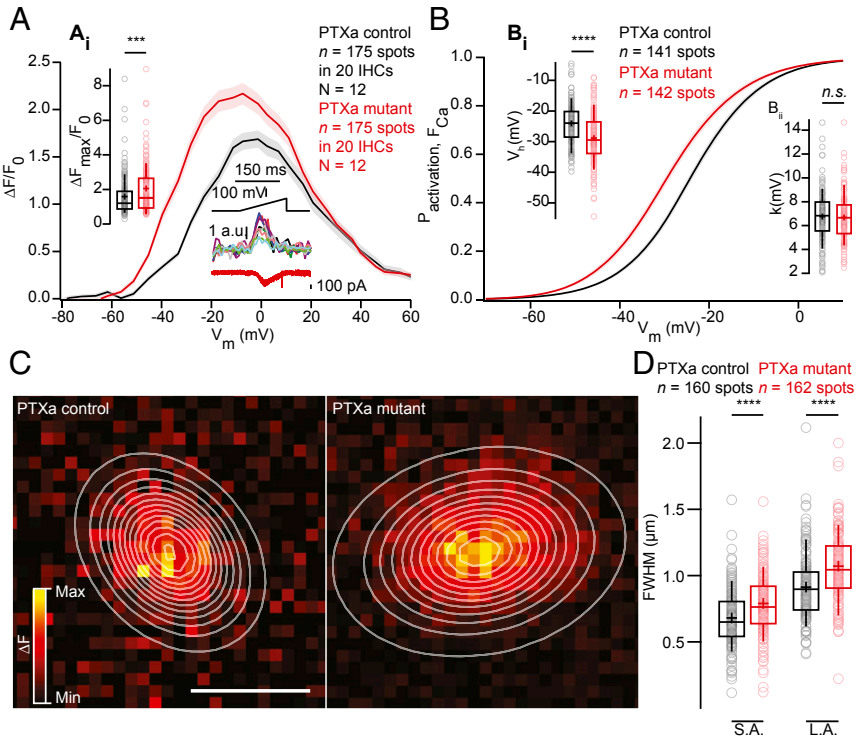

Fig. 5. PTXa-expressing IHCs possess an increased, more spread-out and hyperpolarized Ca^{2+} influx at the single-synapse level. (*A*) FV relationship ($\Delta F/F_0$ vs. depolarization level in ramp), approximating the voltage dependence of synaptic Ca^{2+} influx. Voltage ramps from −87 to +63 mV during 150 ms were used to trigger synaptic hotspots of Fluo-4FF fluorescence and IHC Ca^{2+} influx (in the middle at the bottom; 10 AZs in one exemplary IHC). (A_i) $\Delta F_{max}/F_0$ was calculated by averaging five values at the FV peak and was significantly increased in the PTXa mutant condition ($n = 175$ AZs in 20 IHCs, N = 12 in the PTXa mutant; $n = 175$ AZs in 20 IHCs, N = 12 in the PTXa control; $P = 0.0002$, Mann–Whitney–Wilcoxon test). Mean (line) ± SEM (shaded areas) are displayed; the box plots show 10th, 25th, 50th, 75th, and 90th percentiles with individual data points overlaid, and means are shown as crosses, as for *B* and *D*. (*B*) Fractional activation curves derived from fits to the FV relationships (*C*) were fitted to a Boltzmann function. (B_i) The voltage for half-maximal activation V_h was significantly hyperpolarized in the mutant condition ($n = 142$ AZs in 20 IHCs, N = 12 in the PTXa mutant; $n = 141$ AZs in 20 IHCs, N = 12 in the PTXa control; $P < 0.0001$, Mann–Whitney–Wilcoxon test), while the voltage sensitivity (B_{ii}) did not differ significantly between both conditions ($n = 142$ AZs in 20 IHCs, N = 12 in the PTXa mutant; $n = 141$ AZs in 20 IHCs, N = 12 in the PTXa control; $P = 0.55$, Mann–Whitney–Wilcoxon test). (*C*) Exemplary ΔF pictures of Fluo-4FF hotspots at PTXa control (*Left*) and mutant (*Right*) synapses fitted and overlaid by 2D Gaussian functions to estimate spatial extent as FWHM for the S.A. and the L.A. (*D*) AZs of PTXa mutant IHCs showed a greater spatial spread of the Fluo-4FF fluorescence changes. FWHM calculated from the Gaussian fitting to the Fluo-4FF fluorescence hotspot was larger for both short and long axes in PTXa mutant IHCs ($n = 162$ AZs for 20 IHCs, N = 12) compared with PTXa control ones ($n = 160$ AZs for 20 IHCs, N = 12) ($P < 0.0001$, Mann–Whitney–Wilcoxon test for both axes).

IHCs, N = 12, $P < 0.0001$, Mann–Whitney–Wilcoxon test for both axis] (Fig. 5 *C* and *D*). This larger spread of the presynaptic Ca^{2+} signals is in agreement with the higher prevalence of AZs with multiple Ca^{2+}-channel clusters in PTXa-expressing IHCs.

The Modiolar–Pillar Gradient of Maximal Synaptic Ca^{2+} Influx Is Lost upon PTXa Expression, but the Pillar–Modiolar Gradient of Its Voltage-Dependent Activation Is Maintained. By reconstructing the imaged IHCs as cylindrical models, we then studied the position dependence of AZ properties in live imaging experiments as previously described (14). At P14-18 a tendency for a stronger maximal Ca^{2+} influx was found for modiolar AZs, which also showed a significantly more depolarized activation of the Ca^{2+} channels. Performing this analysis on the synaptic Ca^{2+} influx of PTXa control and mutant IHCs at P21-26, as expected, we found a stronger $\Delta F/F_{max}$ for modiolar than for pillar AZs in PTXa control IHCs [modiolar, 1.68 ± 0.11 (SD = 1.17), $n = 104$ AZs vs. pillar, 1.39 ± 0.11 (SD = 0.91), $n = 65$ AZs in 19 IHCs, N = 11, $P = 0.033$, Mann–Whitney–Wilcoxon test]. PTXa expression completely collapsed this gradient [modiolar, 1.96 ± 0.13 (SD = 1.32), $n = 98$ AZs vs. pillar, 1.94 ± 0.17 (SD = 1.31), $n = 57$ AZs in 18 IHCs, N = 10, $P = 0.91$, Mann–Whitney–Wilcoxon test] (Fig. 6*A*). The "winning" AZs, defined for each cell as the synapse exhibiting the strongest Ca^{2+} influx (highlighted in blue in the box plot and polar charts), were in great majority positioned on the modiolar side in PTXa control IHCs, as previously described (14). In contrast, their localization seemed more random in PTXa-expressing IHCs. However, there was no significant difference in their average positions along the modiolar–pillar axis ($P = 0.10$, *t* test) (*SI Appendix*, Fig. S4) and their respective contributions (ratio between mean $\Delta F/F_{max}$ of winner/mean $\Delta F/F_{max}$ of the rest of the AZs) for a given cell [PTXa mutant, 2.49 ± 0.18 (SD = 0.78) vs. PTXa control, 2.27 ± 0.24 (SD = 1.08), $P = 0.46$, *t* test]. In contrast to the $\Delta F/F_{max}$ gradient, the pillar–modiolar gradient for the V_h of Ca^{2+}-channel activation was maintained in PTXa expressing IHCs [PTXa mutant, modiolar, −26.35 ± 0.83 mV (SD = 7.50 mV), $n = 80$ AZs vs. pillar, −30.64 ± 1.47 mV (SD = 9.57 mV), $n = 42$ AZs in 18 IHCs, N = 10; $P = 0.013$ vs. PTXa control, modiolar, −23.19 ± 0.74 mV (SD = 6.69 mV), $n = 81$ AZs vs. pillar, −25.70 ± 0.96 mV (SD = 6.96 mV), $n = 53$ AZs in 19 IHCs, N = 11; $P = 0.039$, *t* test for both conditions] (Fig. 6*B*).

Discussion

The auditory system processes sound pressures ranging over six orders of magnitude. SGNs with different and complementary firing properties work together to encode this wide dynamic range of audible sounds. Despite progress in defining mechanisms, the functional diversity of SGNs remains largely enigmatic. Defining where the primary mechanism resides and how it is established and maintained are active fields of research. Here we investigated whether Gαi-LGN function, known to influence cell-intrinsic planar polarity at the apex of the HCs, also affects the

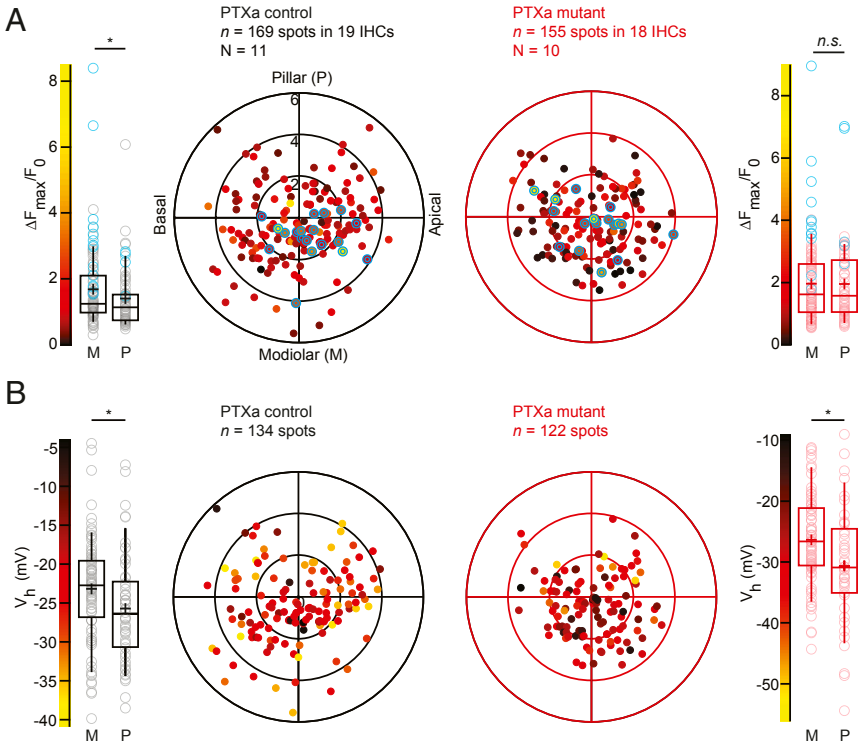

Fig. 6. The modiolar–pillar gradient for synaptic Ca^{2+} influx strength is collapsed upon PTXa expression, but the gradient for voltage-dependent activation is preserved. (*A*) The polar charts display intensities of maximal AZ Ca^{2+} influx ($\Delta F_{max}/F_0$) as a function of AZ positions in live-imaging experiments. Modiolar and pillar refer to facing toward or away from the ganglion in the modiolus; apical and basal refer to the tonotopic axis of the organ of Corti, as for *B*. Box plots of the $\Delta F_{max}/F_0$ and $\Delta F_{max}/F_0$ estimates of individual IHCs show that the PTXa control conditions exhibit significantly stronger Ca^{2+} hotspots in the modiolar side compared with the pillar side (PTXa control, modiolar, $n = 104$ AZs; pillar, $n = 65$ AZs, $P = 0.033$, Mann–Whitney–Wilcoxon test), whereas this gradient is completely collapsed in the PTXa mutant (PTXa mutant, modiolar, $n = 98$ AZs; pillar, $n = 57$ AZs, $P = 0.91$, Mann–Whitney–Wilcoxon test). The strongest AZs from each cell are highlighted in blue in both polar charts and box plots. Data were pooled from 19 and 18 IHCs in PTXa control and mutant conditions, respectively; box plots show 10th, 25th, 50th, 75th, and 90th percentiles with individual data points overlaid; each radial circle is 2 μm, and means are shown as crosses, as for *B*. (*B*) The polar charts display voltages for half-maximal activation V_h as a function of AZ positions in live-imaging experiments. Box plots of the voltage for half-maximal activation V_h and V_h estimates of individual IHCs show a significant hyperpolarized shift of the fractional activation of the $Ca_V1.3$ channels in the pillar side compared with the modiolar side in both control and mutant conditions (PTXa mutant, modiolar, $n = 80$ AZs; pillar, $n = 42$ AZs, $P = 0.013$; PTXa control, modiolar, $n = 81$ AZs; pillar, $n = 53$ AZs, $P = 0.039$; *t* test for both conditions).

presynaptic heterogeneity at the base of IHCs. Interestingly, disrupting Gαi activity via PTXa expression in IHCs collapsed the modiolar–pillar gradients of ribbon size and maximal synaptic Ca^{2+} influx, while reorganizing and enlarging the synapses. Indeed, we found larger and more complex Ca^{2+}-channel clusters by immunofluorescence microscopy, which was corroborated by the observation of increased Ca^{2+} influx at the whole-cell and single-synapse levels. Importantly, PTXa consistently disrupted the modiolar–pillar gradient of ribbon size regardless of IHC planar orientation. Since inactivation of Gαi3 or its binding partner LGN do not affect HC orientation but also disrupted the modiolar–pillar gradient of ribbon size, we suggest that reliance on Gαi function differs to polarize apical and basal IHC features. This could potentially be explained by a strict requirement for Gαi3 to establish the ribbon gradient, while the apical cytoskeleton might be redundantly oriented by multiple Gαis. Overall, our results suggest that Gαi3-LGN participates in establishing the position-dependent properties of IHC AZs.

A Role for Gαi in Setting Up the Spatial Gradient of AZ Properties in IHCs. Although it is well established that PTXa specifically ADP-ribosylates and impairs Gαi function (35), PTXa might affect IHC development in more ways than strictly disrupting planar polarity mechanisms. While the enlarged synaptic Ca^{2+} influx observed upon PTXa argues against decreased IHC fitness or impaired IHC activity, simultaneous disruption of Gαi2 and Gαi3 was reported to impair IHC maturation (26). This conclusion was based on the absence of large-conductance Ca^{2+}-activated K^+ (BK) channels at the IHC neck and the persistence of small-conductance Ca^{2+}-activated K^+ (SK2) channels present before hearing onset and juxtaposed to efferent boutons. PTXa-expressing as well as LGN KO IHCs showed variable BK signals from IHC to IHC ranging from normal clustering to no signal (*SI Appendix*, Fig. S5 *B* and *C*). Agreeing with this mosaic BK expression, SK2 channels ubiquitously present at P7 were observed in a fraction of PTXa expressing IHCs at P22 but were completely absent in littermate controls (*SI Appendix*, Fig. S6 *A–C*). However, several observations argue against a leading role of delayed IHC maturation on the observed PTXa mutant synaptic phenotype. Gαi3 mutant IHCs lost their modiolar–pillar gradient for ribbon size but exhibited a clustering of BK channels at their neck (*SI Appendix*, Fig. S5*A*). Supportive evidence also includes the report of a significant gradient in immature IHCs before hearing onset (27). Moreover, targeted inactivation of the Gαi3-binding partner LGN also collapsed the gradient of the size of synaptic ribbons, suggesting that the similar collapse upon PTXa likely reflects defective Gαi3-LGN cell polarization. While the increased whole-cell Ca^{2+} current per se could be consistent with impaired IHC maturation (e.g., ref. 36), further arguments against a major maturational deficit include (*i*) a qualitatively similar amount of extrasynaptic $Ca_V1.3$ Ca^{2+} channels at the confocal level as well as a comparable maximal Ca^{2+} influx potentiation in PTXa mutants at the whole-cell and synapse levels (30 and 23%, respectively); (*ii*) well-defined PSDs at the confocal and STED levels, in contrast to the several small PSDs per contact found at earlier stages (28); (*iii*) same ribbon intensity and number, while more and smaller ribbons were found in immature IHCs; and finally, (*iv*) stronger synaptic Ca^{2+} influx, while weaker Ca^{2+} influx per AZ was found before hearing onset (28). Altogether, Gαi signaling could thus be required for aspects of IHC maturation independently from its role in diversifying ribbon synapse properties. In conclusion, our results strongly suggest that Gαi-LGN signaling directly regulates the modiolar–pillar gradient of synapse properties.

Considering other possible confounding mechanisms, it is worth noting that stunted and disorganized stereocilia affecting hair bundle function and thus sound encoding per se are unlikely to alter synapses, as we did not find obvious changes in position-dependent morphological synapse properties in *Myo15*^{sh2} mutants. Nonetheless, some aspects of the synaptic phenotype observed in the PTXa mutant IHCs are reminiscent of the USH1C deaf-circler mutant mice, where absence of the harmonin protein induces severe hair bundle defects. There, too, an increased amplitude and hyperpolarized activation of synaptic Ca^{2+} influx was observed, but no evidence for an immaturity phenotype was found (14). A gain of synaptic function through increased number and more hyperpolarized activation of Ca^{2+} channels could be a mechanism to increase spontaneous SGN firing to compensate for the lack of sound-evoked firing. Hence, the potentiated Ca^{2+} influx could be secondary to a deficit of mechanotransduction.

Candidate Mechanisms for Defining Position-Dependent AZ Ca^{2+} Influx Properties. Using single-cell RNA sequencing, recent studies (37–39) characterized three distinct subpopulations of type I SGNs in the mouse. Interestingly, these transcriptome-based subpopulations expressed distinct complements of transcription factors but also ion channels, receptors, and synaptic proteins. Moreover, as these different subpopulations were shown to differentially target the IHC basolateral periphery, their profiling offered potential postsynaptic determinants that could account for heterogeneous firing properties of the SGNs. Moreover, these SGN subpopulations might exert differential instructive influence on the properties of presynaptic IHC AZs. By reconstructing the patch-clamped cells we found that blocking Gαi signaling abolishes the modiolar–pillar gradient for the maximal strength of synaptic Ca^{2+} influx but preserves the pillar–modiolar gradient for the voltage dependence of Ca^{2+} channel activation. This finding might indicate that distinct mechanisms govern the spatial distribution of the number of Ca^{2+} channels per AZ and their voltage dependence of activation. This observation of unchanged spatial gradient of voltage dependence of activation would be consistent with observations in IHCs of Gipc3 KO mice, where the gradient for the strength of synaptic Ca^{2+} influx was reversed, while the pillar–modiolar one for voltage dependence of activation was maintained (14). The mutated Gipc3^{343A} allele disrupts the hair bundle structure and leads to progressive sensorineural hearing loss (40). Gipc1 was shown to interact with the core PCP protein Vangl2, and its disruption leads to maturation defects affecting hair bundle orientation and integrity (41). Interestingly, an interaction between Gipc1 and Tyrosine kinase receptor TrkA was described in culture, proposing Gipc1 as a link between TrkA and G protein signaling (42). Candidate mechanisms defining the voltage dependence of activation at a given AZ include the precise splice $Ca_V1.3$ variant(s) (14, 43, 44), the subunit composition (45), and interacting proteins present (14, 34, 46, 47).

Several studies in the neuromast HCs of larval zebrafish, including modified expression of RIBEYE (48, 49) and frame shift *ribeye* mutations (50), as well as Cre-deletion of RIBEYE in the mouse cochlea and retina (34, 51, 52), have shown a relationship between the ribbon and the Ca^{2+}-channel cluster organization. A depolarized shift of the voltage dependence activation of Ca^{2+} influx was found in RIBEYE-deficient IHCs (34), but a direct interaction of RIBEYE and the Ca^{2+} channel complex has not yet been reported. Aside from RIBEYE, Bassoon has been shown to promote Ca^{2+}-channel tethering at the AZ (53) likely via interaction with RIM-binding protein (54). RIM-binding protein was reported to interact with $Ca_V1.3$ Ca^{2+} channels (55) and is necessary to establish a normal Ca^{2+}-channel complement at the IHC AZ (56). Moreover, RIM2α and β have been reported to promote the clustering of these channels at the synapse (47), and RIM2 and RIM3 were shown to directly interact with the pore-forming subunit of $Ca_V1.3$ Ca^{2+} channel (57). It will be of interest to explore possible interactions determining whether the trafficking of these different AZ proteins are governed by the Gαi3-LGN complex. Future experiments are required to investigate the importance of LGN for synaptic physiology and identify potential alternative interacting partners for Gαi besides LGN, including membrane receptors or other planar polarity protagonists. In particular, it will be interesting to ask whether tissue-level mechanisms regulating IHC planar orientation at cell–cell junctions (e.g., core PCP proteins)

also influence the spatial gradient of ribbon size and/or synaptic physiology. In addition, emphasis should be put on ultrastructural studies by electron microscopy to further characterize the spatial reorganization of the synapses, as well as recordings from auditory nerve fibers to assess the effect on the SGN firing rate diversity.

Materials and Methods

All experiments complied with national animal care guidelines and were approved by the University of Göttingen Board for Animal Welfare, the Animal Welfare Office of the State of Lower Saxony, and the Animal Care and Use Committee of The Jackson Laboratory. For details of patch-clamp and confocal Ca^{2+} imaging, immunohistochemistry and confocal/STED imaging, and data analysis, see *SI Appendix, SI Materials and Methods*.

ACKNOWLEDGMENTS. We thank Gerhard Hoch for developing MATLAB programs for image analysis and Sandra Gerke as well as Christiane Senger-Freitag for expert technical assistance. This work was supported by the National Institute on Deafness and Other Communication Disorders (R01 DC015242 to B.T.) and grants of the German Research Foundation through the Collaborative Research Center 889 (Project A8 to T.M.), the Cluster of Excellence and Research Center for Nanoscale Microscopy and Molecular Physiology of the Brain (EXC171/FZT103), the Leibniz Program (T.M.), and the Max-Planck-Society (Max-Planck-Fellowship to T.M.).

1. Russell IJ, Sellick PM (1983) Low-frequency characteristics of intracellularly recorded receptor potentials in guinea-pig cochlear hair cells. *J Physiol* 338:179–206.
2. Liberman MC (1978) Auditory-nerve response from cats raised in a low-noise chamber. *J Acoust Soc Am* 63:442–455.
3. Ohlemiller KK, Echteler SM, Siegel JH (1991) Factors that influence rate-versus-intensity relations in single cochlear nerve fibers of the gerbil. *J Acoust Soc Am* 90: 274–287.
4. Winter IM, Robertson D, Yates GK (1990) Diversity of characteristic frequency rate-intensity functions in guinea pig auditory nerve fibres. *Hear Res* 45:191–202.
5. Liberman MC (1982) Single-neuron labeling in the cat auditory nerve. *Science* 216: 1239–1241.
6. Merchan-Perez A, Liberman MC (1996) Ultrastructural differences among afferent synapses on cochlear hair cells: Correlations with spontaneous discharge rate. *J Comp Neurol* 371:208–221.
7. Yin Y, Liberman LD, Maison SF, Liberman MC (2014) Olivocochlear innervation maintains the normal modiolar-pillar and habenular-cuticular gradients in cochlear synaptic morphology. *J Assoc Res Otolaryngol* 15:571–583.
8. Liberman LD, Wang H, Liberman MC (2011) Opposing gradients of ribbon size and AMPA receptor expression underlie sensitivity differences among cochlear-nerve/hair-cell synapses. *J Neurosci* 31:801–808.
9. Zhang L, Engler S, Koepcke L, Steenken F, Köppl C (2018) Concurrent gradients of ribbon volume and AMPA-receptor patch volume in cochlear afferent synapses on gerbil inner hair cells. *Hear Res* 364:81–89.
10. Ruel J, et al. (2001) Dopamine inhibition of auditory nerve activity in the adult mammalian cochlea. *Eur J Neurosci* 14:977–986.
11. Meyer AC, et al. (2009) Tuning of synapse number, structure and function in the cochlea. *Nat Neurosci* 12:444–453.
12. Frank T, Khimich D, Neef A, Moser T (2009) Mechanisms contributing to synaptic Ca2+ signals and their heterogeneity in hair cells. *Proc Natl Acad Sci USA* 106:4483–4488.
13. Kantardzhieva A, Liberman MC, Sewell WF (2013) Quantitative analysis of ribbons, vesicles, and cisterns at the cat inner hair cell synapse: Correlations with spontaneous rate. *J Comp Neurol* 521:3260–3271.
14. Ohn T-L, et al. (2016) Hair cells use active zones with different voltage dependence of Ca2+ influx to decompose sounds into complementary neural codes. *Proc Natl Acad Sci USA* 113:E4716–E4725.
15. Goodrich LV, Strutt D (2011) Principles of planar polarity in animal development. *Development* 138:1877–1892.
16. Lu X, Sipe CW (2016) Developmental regulation of planar cell polarity and hair-bundle morphogenesis in auditory hair cells: Lessons from human and mouse genetics. *Wiley Interdiscip Rev Dev Biol* 5:85–101.
17. Montcouquiol M, Kelley MW (January 7, 2019) Development and patterning of the cochlea: From convergent extension to planar polarity. *Cold Spring Harb Perspect Med*, 10.1101/cshperspect.a033266.
18. Tarchini B, Jolicoeur C, Cayouette M (2013) A molecular blueprint at the apical surface establishes planar asymmetry in cochlear hair cells. *Dev Cell* 27:88–102.
19. Bergstralh DT, Dawney NS, St Johnston D (2017) Spindle orientation: A question of complex positioning. *Development* 144:1137–1145.
20. Ezan J, et al. (2013) Primary cilium migration depends on G-protein signalling control of subapical cytoskeleton. *Nat Cell Biol* 15:1107–1115.
21. Siletti K, Tarchini B, Hudspeth AJ (2017) Daple coordinates organ-wide and cell-intrinsic polarity to pattern inner-ear hair bundles. *Proc Natl Acad Sci USA* 114: E11170–E11179.
22. Mauriac SA, et al. (2017) Defective Gpsm2/$G\alpha_{i3}$ signalling disrupts stereocilia development and growth cone actin dynamics in Chudley-McCullough syndrome. *Nat Commun* 8:14907.
23. Tarchini B, Tadenev ALD, Devanney N, Cayouette M (2016) A link between planar polarity and staircase-like bundle architecture in hair cells. *Development* 143: 3926–3932.
24. Tadenev ALD, et al. (2019) GPSM2-GNAI specifies the tallest stereocilia and defines hair bundle row identity. *Curr Biol* 29:921–934.e4.
25. Bhonker Y, et al. (2016) The GPSM2/LGN GoLoco motifs are essential for hearing. *Mamm Genome* 27:29–46.
26. Beer-Hammer S, et al. (2018) Gαi proteins are indispensable for hearing. *Cell Physiol Biochem* 47:1509–1532.
27. Liberman LD, Liberman MC (2016) Postnatal maturation of auditory-nerve heterogeneity, as seen in spatial gradients of synapse morphology in the inner hair cell area. *Hear Res* 339:12–22.
28. Wong AB, et al. (2014) Developmental refinement of hair cell synapses tightens the coupling of Ca2+ influx to exocytosis. *EMBO J* 33:247–264.
29. Probst FJ, et al. (1998) Correction of deafness in shaker-2 mice by an unconventional myosin in a BAC transgene. *Science* 280:1444–1447.
30. Platzer J, et al. (2000) Congenital deafness and sinoatrial node dysfunction in mice lacking class D L-type Ca2+ channels. *Cell* 102:89–97.
31. Brandt A, Striessnig J, Moser T (2003) CaV1.3 channels are essential for development and presynaptic activity of cochlear inner hair cells. *J Neurosci* 23:10832–10840.
32. Dou H, et al. (2004) Null mutation of alpha1D Ca2+ channel gene results in deafness but no vestibular defect in mice. *J Assoc Res Otolaryngol* 5:215–226.
33. Neef J, et al. (2018) Quantitative optical nanophysiology of Ca^{2+} signaling at inner hair cell active zones. *Nat Commun* 9:290.
34. Jean P, et al. (2018) The synaptic ribbon is critical for sound encoding at high rates and with temporal precision. *eLife* 7:e29275.
35. Locht C, Coutte L, Mielcarek N (2011) The ins and outs of pertussis toxin. *FEBS J* 278: 4668–4682.
36. Sendin G, Bulankina AV, Riedel D, Moser T (2007) Maturation of ribbon synapses in hair cells is driven by thyroid hormone. *J Neurosci* 27:3163–3173.
37. Petitpré C, et al. (2018) Neuronal heterogeneity and stereotyped connectivity in the auditory afferent system. *Nat Commun* 9:3691.
38. Shrestha BR, et al. (2018) Sensory neuron diversity in the inner ear is shaped by activity. *Cell* 174:1229–1246.e17.
39. Sun S, et al. (2018) Hair cell mechanotransduction regulates spontaneous activity and spiral ganglion subtype specification in the auditory system. *Cell* 174:1247–1263.e15.
40. Charizopoulou N, et al. (2011) Gipc3 mutations associated with audiogenic seizures and sensorineural hearing loss in mouse and human. *Nat Commun* 2:201.
41. Giese AP, et al. (2012) Gipc1 has a dual role in Vangl2 trafficking and hair bundle integrity in the inner ear. *Development* 139:3775–3785.
42. Lou X, Yano H, Lee F, Chao MV, Farquhar MG (2001) GIPC and GAIP form a complex with TrkA: A putative link between G protein and receptor tyrosine kinase pathways. *Mol Biol Cell* 12:615–627.
43. Bock G, et al. (2011) Functional properties of a newly identified C-terminal splice variant of Cav1.3 L-type Ca2+ channels. *J Biol Chem* 286:42736–42748.
44. Tan BZ, et al. (2011) Functional characterization of alternative splicing in the C terminus of L-type CaV1.3 channels. *J Biol Chem* 286:42725–42735.
45. Cui G, et al. (2007) Ca2+-binding proteins tune Ca2+-feedback to Cav1.3 channels in mouse auditory hair cells. *J Physiol* 585:791–803.
46. Gregory FD, Pangršič T, Calin-Jageman IE, Moser T, Lee A (2013) Harmonin enhances voltage-dependent facilitation of $Ca_v1.3$ channels and synchronous exocytosis in mouse inner hair cells. *J Physiol* 591:3253–3269.
47. Jung S, et al. (2015) Rab3-interacting molecules 2α and 2β promote the abundance of voltage-gated CaV1.3 Ca2+ channels at hair cell active zones. *Proc Natl Acad Sci USA* 112:E3141–E3149.
48. Sheets L, Trapani JG, Mo W, Obholzer N, Nicolson T (2011) Ribeye is required for presynaptic Ca(V)1.3a channel localization and afferent innervation of sensory hair cells. *Development* 138:1309–1319.
49. Sheets L, et al. (2017) Enlargement of ribbons in zebrafish hair cells increases calcium currents but disrupts afferent spontaneous activity and timing of stimulus onset. *J Neurosci* 37:6299–6313.
50. Lv C, et al. (2016) Synaptic ribbons require ribeye for electron density, proper synaptic localization, and recruitment of calcium channels. *Cell Rep* 15:2784–2795.
51. Becker L, et al. (2018) The presynaptic ribbon maintains vesicle populations at the hair cell afferent fiber synapse. *eLife* 7:e30241.
52. Maxeiner S, Luo F, Tan A, Schmitz F, Südhof TC (2016) How to make a synaptic ribbon: RIBEYE deletion abolishes ribbons in retinal synapses and disrupts neurotransmitter release. *EMBO J* 35:1098–1114.
53. Frank T, et al. (2010) Bassoon and the synaptic ribbon organize Ca^2+ channels and vesicles to add release sites and promote refilling. *Neuron* 68:724–738, and erratum (2010) 68:1202.
54. Davydova D, et al. (2014) Bassoon specifically controls presynaptic P/Q-type Ca(2+) channels via RIM-binding protein. *Neuron* 82:181–194.
55. Hibino H, et al. (2002) RIM binding proteins (RBPs) couple Rab3-interacting molecules (RIMs) to voltage-gated Ca(2+) channels. *Neuron* 34:411–423.
56. Krinner S, Butola T, Jung S, Wichmann C, Moser T (2017) RIM-binding protein 2 promotes a large number of CaV1.3 Ca2+-channels and contributes to fast synaptic vesicle replenishment at hair cell active zones. *Front Cell Neurosci* 11:334.
57. Picher MM, et al. (2017) Rab interacting molecules 2 and 3 directly interact with the pore-forming $Ca_V1.3$ Ca^{2+} channel subunit and promote its membrane expression. *Front Cell Neurosci* 11:160.